Piezo-enhanced charge carrier separation over plasmonic Au-BiOBr for piezo-photocatalytic carbamazepine removal

Jiayue Hu [a], Yanxi Chen [a], Yuanyi Zhou [a], Lixi Zeng [a,*], Yichao Huang [b,*], Shenyu Lan [a], Mingshan Zhu [a,c,**]

[a] Guangdong Key Laboratory of Environmental Pollution and Health, School of Environment, Guangdong-Hongkong-Macau Joint Laboratory of Collaborative Innovation for Environmental Quality, Jinan University, Guangzhou 511443, PR China
[b] Department of Toxicology, School of Public Health, Anhui Medical University, Hefei 230032, PR China
[c] State Key Laboratory of Urban Water Resource and Environment, Harbin Institute of Technology, Harbin 150090, PR China

ABSTRACT

The piezo-photocatalytic effect of Au decorated bismuth oxybromide (BiOBr) was investigated to elucidate the regulation of built-in electric field on charge carrier dynamics and exploit the potential of multi-field coupled environmental purification. Physicochemical properties of Au-BiOBr such as the piezoelectricity, photoresponse characteristics, and charge separation efficiencies were thoroughly analyzed, meanwhile the degradation of carbamazepine (CBZ) was chosen to evaluate the catalytic performance of this system. The piezo-photocatalytic removal of CBZ reached 95.8% within 30 min, and the rate constant is 1.73 times higher than the sum of individual piezo- and photocatalytic ones. The results attribute to not only the modification of Au nanoparticles that accelerates charge transfer and improves light absorption, but also, more importantly, the piezoelectric effect of BiOBr that amplifies the built-in electric field and modulates the band structure alignment. This work demonstrates a promising environmental remediation strategy via the co-utilization of solar and mechanical energy in nature.

1. Introduction

The built-in electric field of material is critical to the separation and migration of charge carriers, which plays an important role in improving energy conversion and environment remediation efficiency [1–5]. In addition to interface engineering (heterojunctions, Schottky junctions, p-n junctions, etc.), the application of multi-field coupling energy is also an effective strategy to regulate the built-in electric field [5–7]. In particular, piezo-photocatalysis arises as an ideal model of charge separation promoted by the built-in electric field. On one hand, light irradiation ensures the generation of charge carriers [8,9]. On the other hand, mechanical stress accelerates the separation of charge carriers. With the reactivity outperforming piezo- and photocatalysis solely, piezo-photocatalysis has attracted extensive research interest recently [10–12].

Bismuth oxybromide (BiOBr) is a competent candidate for piezo-photocatalysis prized for its unique structural and physicochemical

properties [13,14]. The interleaved $[Bi_2O_2]^{2+}$ and Br^- slabs along [001] direction endows BiOBr its piezoelectricity [15–18]. The intrinsic built-in electric field of BiOBr would be further enhanced under mechanical stress to boost charge separation [19–21]. Besides, the band structure alignments of BiOBr are also positioned properly, which could realize the activation of small molecules (H_2O, O_2, etc.) and produce reactive oxygen species under light irradiation [21–23]. Based on these characteristics, a rational design of BiOBr is expected to achieve the coupling of piezo- and photocatalysis (i.e., piezo-photocatalysis) for efficient energy capture and utilization.

In this work, we investigated the piezo-photocatalytic effect of Au modified BiOBr on the degradation of environmentally persistent contaminant. The built-in electric field within BiOBr was greatly enhanced under the application of mechanical stress, which both accelerated charge transfer and regulated the band structure alignments. Au decoration improved visible light absorption, meanwhile accelerating charge transfer. Carbamazepine (CBZ), one of the common

---

pharmaceutical and personal care products, was chosen as a model contaminant to evaluate the piezo-photocatalytic performance of Au-BiOBr. The outstanding piezo-photocatalytic performance in comparison to the piezo- or photocatalytic approach alone demonstrated piezo-photocatalysis as an efficient technology for environmental purification.

2. Materials and methods

2.1. Synthesis of catalysts

BiOBr nanosheets were prepared by a simple hydrothermal procedure. 8 mmol $Bi(NO_3)_3.5H_2O$ (3.88 g) and 8 mmol (0.952 g) KBr were dissolved in 40 mL distilled water, respectively. Then, the KBr solution was added dropwise to the $Bi(NO_3)_3$ solution under vigorous stirring. The combined solution was placed to a 100 mL Teflon autoclave and heated to 160 °C for 12 h after stirring for 30 min. The generated sediment was thoroughly cleaned with distilled water and ethanol, and was subsequently dried in air at 60 °C for 12 h.

Au nanoparticles (Au NPs) were loaded on BiOBr by the photo-reduction method. 300 mg BiOBr and 0.03, 0.06 or 0.3 mL $HAuCl_4$ (0.0254 M) were added in 40 mL water including 20% ($V_{methanol}/V_{water}$) methanol in the 100 mL glass tube, respectively. Then, under magnetic stirring, the sample was irradiated for 1 h under UV radiation. The precipitates were separated by centrifugation and washed completely with water and ethanol before being dried in a vacuum oven at 60 °C overnight. The loading amounts of Au decorated on the surface of BiOBr nanostructures were 0.05, 0.1, and 0.5 wt%, respectively. The catalyst preparation method is depicted in Fig. S1. Detailed chemicals information involved in the experiments are provided in the Supporting information. The UV absorption spectra of $HAuCl_4$/BiOBr solution at different photo-reduction times were measured to detect whether $AuCl_4^-$ metal ions were reduced. As can be seen from Fig. S2, the absorption peak of $HAuCl_4$ solution is 302 nm, which is mainly attributed to the absorption of Au^{3+}. However, after 60 min of photo-reduction reaction, the absorption peak at 302 nm disappeared, which proved that Au^{3+} have been all reduced to Au NPs. Assuming a 100% photo reduction efficiency, the loading amounts of Au decorated on the surface of BiOBr nanosheets are 0.1 wt%.

2.2. Characterization of catalysts

The details for various characterization technologies are provided in the Supporting information.

2.3. Experimental procedure and analysis methods

All experiments were done in a 100 mL beaker. The visible (Vis) light source was a 300 W Xenon light source (PLS-SXE300D, Beijing Perfectlight Technology Co., Ltd) with a 400 nm cutoff filter. The mechanical force to distort Au-BiOBr to create a piezoelectric effect was provided by an ultrasonic (US) cleaner (40 kHz, 100 W, Mojie, Dongguan, China). High-performance liquid chromatography was used to determine the concentration of CBZ (HPLC, Shimadzu LC-16). The mobile phases were acetonitrile and 0.1% formic acid in a 40%: 60% in water, and the HPLC was fitted with a diode array detector at 254 nm. The degradation products were identified in the mass range of 50–500 m/z using a liquid chromatography/time-of-flight/mass spectrometer (LC-TOF-MS, AB Sciex, LC-Triple-TOF5600) in positive mode (ESI+). The mobile phase was composed of a linear gradient of 0.1% formic acid (A) and acetonitrile (B), eluted at 0.2 mL min^{-1} as follows: raising acetonitrile from 10% to 40% in 1 min and maintaining for 7 min; then increasing acetonitrile from 40% to 90% in 1 min and maintaining for 7 min; equilibrating the column by reducing acetonitrile to 10% in 1 min. Concentrations of CBZ and degradation products were quantified using Analyst® software.

Electron paramagnetic resonance (EPR) spectra equipped with DMPO or TEMP as the spin-trapping agent were detected on a Bruker spectrometer (ESR 5000) in water or dimethyl sulfoxide solution. The electrochemical measurements were carried out in the quartz beaker via an electrochemical workstation CHI 760E (Shanghai Chenhua Instrumental Co., Ltd., China) with three electrodes system, wherein the Au/BiOBr or BiOBr modified electrode was acted as working electrode. Pt wire and saturated calomel electrode (SCE) were acted as counter and reference electrodes, respectively. Schematic of the experimental setup is shown in Scheme 1, CBZ degradation experiments exclude electrochemical acquisition systems.

3. Results and discussion

3.1. Characterization

XRD, Raman, SEM, and TEM characterization were used to analyze the structure and morphology of the as-prepared samples. As shown in Fig. 1A, all diffraction peaks for these materials were indexed as BiOBr (JCPDS card No. 09–0393). Over the Au modified samples, no diffraction peak of Au NPs was noticed, which might be attributed to the low loading quantity [24]. Raman spectroscopy verifies the interaction between Au NPs and BiOBr nanosheets. The strongest band at 112 cm^{-1} was attributed to the A_{1g} internal Bi-Br stretching mode, whereas the band at 162 cm^{-1} was assigned to the E_g internal Bi-Br stretching mode, as illustrated in Fig. 1B [25]. The mobility of oxygen atoms caused the weak bands E_g and B_{1g} at roughly 384 cm^{-1}. The deposited Au NPs caused a substantial redshift [26]. SEM and TEM images (Fig. 1C and 1D) display the nanosheet structure of BiOBr with the size ranging from 0.75 to 3.9 μm. The average diameter of Au NPs was determined to be ca. 20 nm, and they were evenly disseminated on the surface of BiOBr nanosheets. In the high-resolution TEM image (Fig. 1E), clear lattice fringes with the interplanar spacing of 0.23 and 0.27 nm were attributed to the (111) facet of Au NPs and the (110) facet of BiOBr, respectively [27,28].

The interaction between Au NPs and BiOBr nanosheets was investigated using XPS (Fig. 2). Two characteristic peaks situated at 164.9 and 159.6 eV were ascribed to Bi $4f_{5/2}$ and Bi $4f_{7/2}$ (Fig. 2A), while that at 70.3 and 69.2 eV corresponded to Br $3d_{3/2}$ and Br $3d_{5/2}$ (Fig. 2B). The binding energy of 531.4 and 530.6 eV in the O 1s spectra (Fig. 2C) was attributed to the hydroxyl group and crystal lattice oxygen ($[Bi_2O_2]^{2+}$ ionic layer) in the BiOBr nanosheets [29,30]. In the Au 4f spectrum of Au-BiOBr (Fig. 2D), the peaks at 87.6 and 84.0 eV implied the zero-valent state of Au NPs, demonstrating the successful reduction of $AuCl_4^-$ under UV irradiation [31]. Interestingly, after the modification of Au NPs, the binding energies of Bi 4f, Br 3d, and O 1s became lower than that of the pristine sample, the peaks of both samples are identical which can partly elucidate no changes happened in the bulk phase.
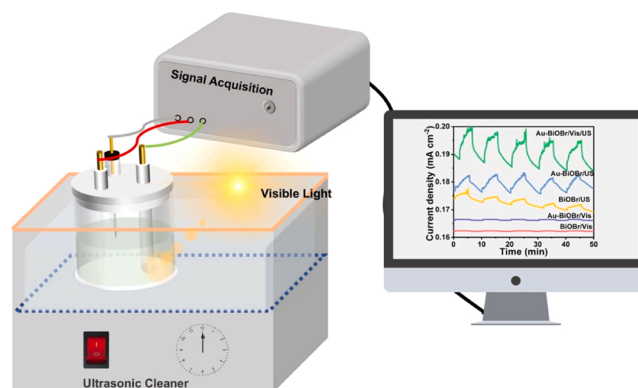
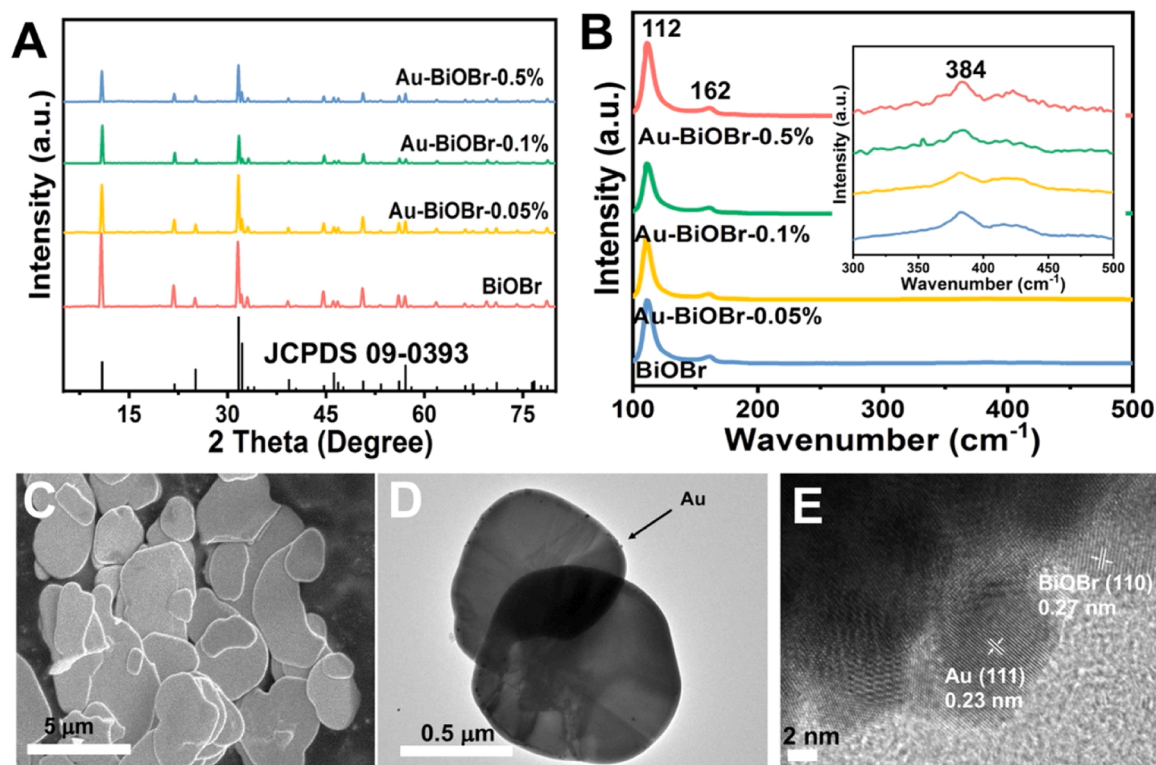**Scheme 1.** Schematic of the piezo-photocatalytic reactor setup.

Fig. 1. (A) XRD patterns and (B) Raman spectra of BiOBr and Au-BiOBr nanocomposites with different weight ratio of Au NPs: 0.05, 0.1, and 0.5 wt%; (C) SEM image of BiOBr nanosheets; (D) TEM image of Au-BiOBr nanocomposites; (E) HRTEM image of Au-BiOBr nanocomposites.
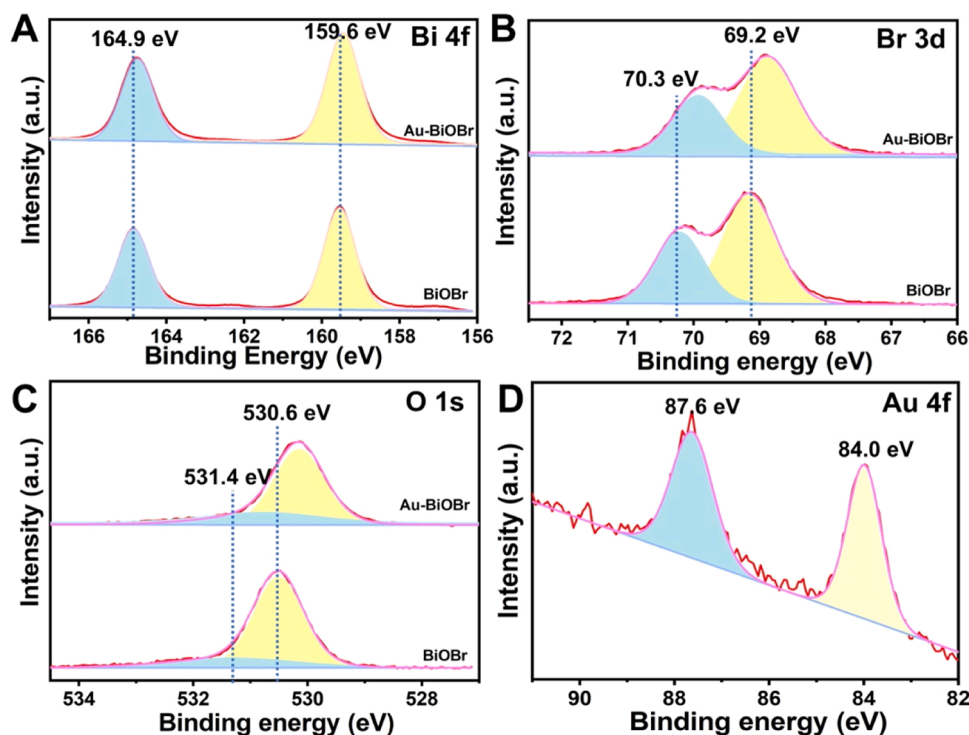

Fig. 2. XPS spectra of Bi 4f (A), Br 3d (B), and O1s (C) of BiOBr and Au-BiOBr nanocomposite. XPS spectra of Au 4f (D) of Au-BiOBr nanocomposite.

3.2. Physicochemical properties

With the basic structural understanding of the as-prepared samples, the piezoelectricity of BiOBr nanosheets was then studied. The 3D height images clearly reveal the surface topography of the BiOBr nanosheets with a very rough surface (Fig. 3A). The PFM phase and amplitude image for BiOBr was shown in Fig. 3B. In the hysteresis loop, the phase angle varied by around 180°, showing local ferroelectric polarization flipping inside BiOBr. The butterfly-shaped amplitude curve was a well-known property of ferroelectric materials, demonstrating ferroelectric/
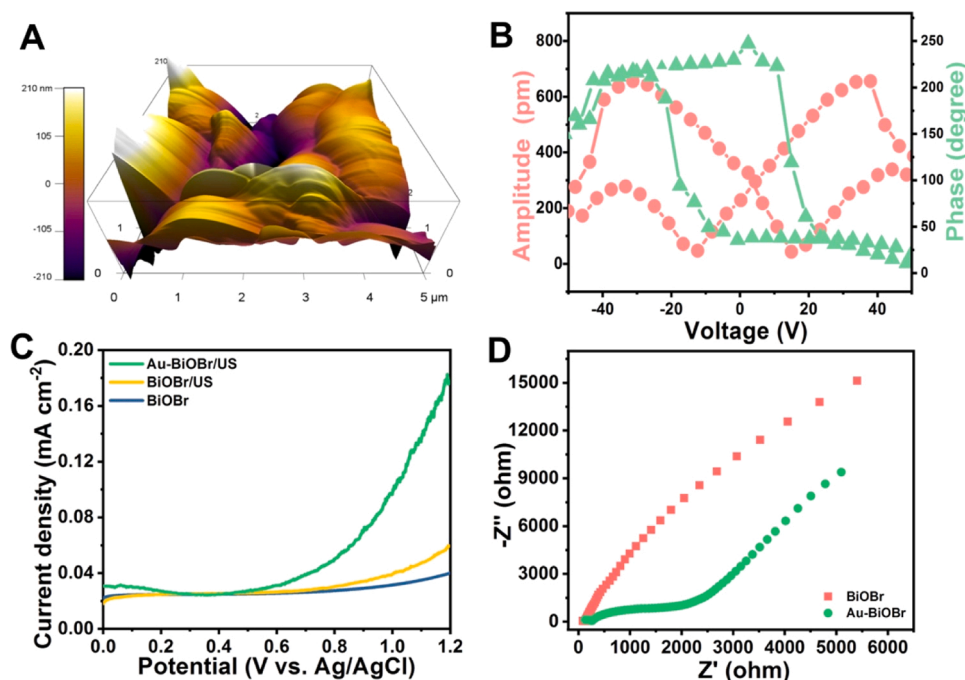
Fig. 3. (A) AFM morphology of BiOBr nanosheets; (B) PFM ferroelectric hysteresis loops of BiOBr nanosheets; (C) Current density versus potential (*J-V*) curve of BiOBr and Au-BiOBr under ultrasonic vibration in 0.5 M Na_2SO_4 solution at a scan rate of 10 mV s^{-1}; (D) EIS spectra of the BiOBr and Au-BiOBr in 2.5 mM K_3[Fe $(CN)_6$]/K_4[Fe(CN)$_6$] + 0.1 M KCl.

piezoelectric nature of BiOBr [32].

Electrochemical characterizations were further carried out to explore the piezoelectricity of BiOBr and the role of Au modification. Under ultrasonic vibration condition, the current intensity of BiOBr nanosheets (Fig. 3C) increased up to 0.036 mA cm^{-2} at the bias of 1.2 V, verifying that BiOBr could respond toward the external mechanical stress and

generate surface charges for piezocatalysis. In addition, the onset potential of BiOBr changed a little under the application of mechanical stress, which implied band bending caused by the piezoelectric effect. After the modification of Au NPs, a much higher current intensity at the bias of 1.2 V (0.176 mA cm^{-2}) was obtained along with a smaller impedance in the electrochemical impedance spectroscopy (Fig. 3D).
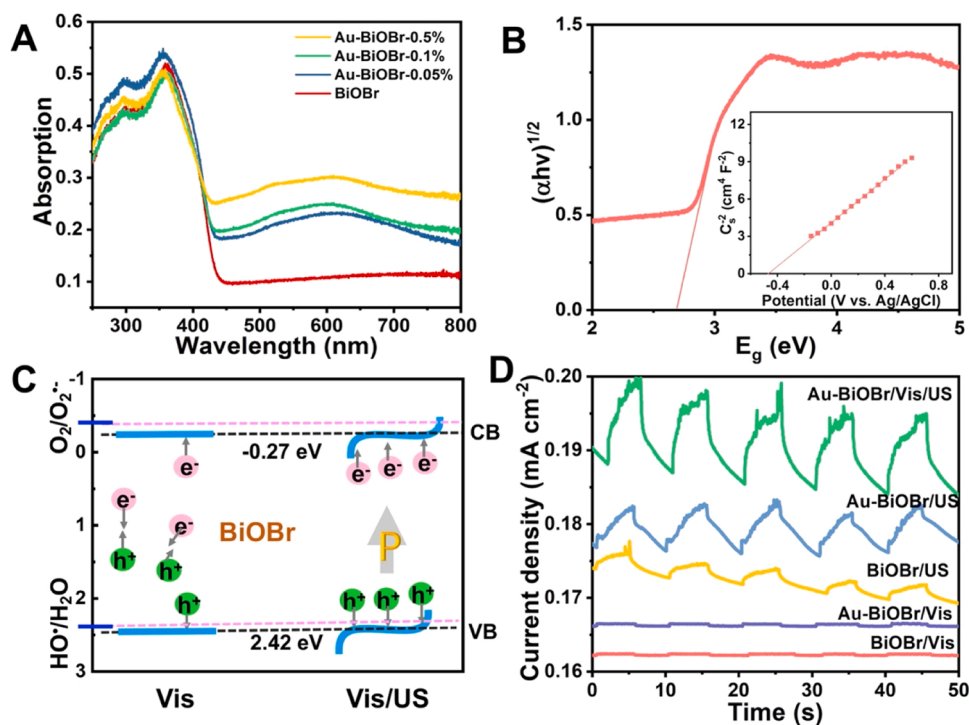

Fig. 4. (A) UV-Vis spectra of BiOBr and Au-BiOBr nanocomposites with different weight ratio of Au NPs: 0.05, 0.1, and 0.5 wt%; (B) The bandgap energy of BiOBr, (Insert: Mott-Schottky plot of the BiOBr nanosheets in 0.5 M Na_2SO_4 solution); (C) Energy bands of BiOBr during photocatalytic and piezo-photocatalytic process; (D) Piezo-current response in 0.5 M Na_2SO_4 solution at 0.8 V.

These results suggested that Au NPs could accelerate piezo-induced electron transfer as excellent electron conductors through the Schottky junction. Therefore, the piezocatalytic effect of BiOBr would be improved after Au deposition.

The photoresponse characteristics of BiOBr nanosheets were also investigated. A typical absorption edge at around 452 nm was observed in UV–vis spectra (Fig. 4A). The surface plasmon resonance (SPR) effect of Au NPs caused a prominent absorption peak at 602 nm after they were decorated. The bandgap (E_g) of BiOBr nanosheets was calculated to be 2.69 eV (Fig. 4B), with valence band (VB) and conduction band (CB) alignments of 2.42 and − 0.27 eV, respectively (Fig. 4C) [33]. Thermodynamically, the VB maximum of BiOBr was more positive than the standard potential of H_2O oxidation ($HO^\bullet/H_2O$, 2.40 eV), thus it was easy for the induced holes to participate in $HO^\bullet$ generation. However, the CB minimum of BiOBr was slightly more positive than the standard potential of $O_2^{\bullet-}$ production ($O_2/O_2^{\bullet-}$, −0.33 eV) [34], so the reduction process was sluggish, and the photocatalytic system would suffer from severe charge recombination (Fig. 4D). When ultrasonic vibration was coupled into the photocatalytic process, the highest current response was achieved over Au-BiOBr (0.193 mA cm^{-2}), which was superior to the individual ultrasonic vibration or visible light irradiation. The apparent current intensity obtained from piezo-photocatalysis demonstrated that the strengthened built-in electric field within Au-BiOBr would not only facilitate charge separation but also moderate the band structure alignment [35]. As a result, the sluggish $O_2^{\bullet-}$ generation process over Au-BiOBr would be improved, as well as the separation efficiency of the charge carriers, and eventually the overall catalytic activity.

3.3. Piezo-photocatalytic degradation of CBZ

From the results above, the considerable current response under the coupling of visible light irradiation and ultrasonic vibration indicated good piezo-photocatalytic performance. The degradation of CBZ was selected as a model reaction to evaluate the system. The piezocatalytic degradation performance over the pristine BiOBr and a series of Au-BiOBr samples were shown in Fig. 5A. The catalysts were distributed in the CBZ aqueous solution by swirling in the dark for 20 min to obtain the adsorption-desorption equilibrium prior to the degradation experiments. Only less than 2% of CBZ was removed by BiOBr or Au-BiOBr, illustrating that the adsorption on the catalyst was negligible. The ultrasonic vibration itself did not induce the change of CBZ concentration without catalyst introduction. Through the piezocatalytic effect of BiOBr, about 9.2% of CBZ was removed after ultrasonic vibration. The efficiency was boosted to 66.2% after loading 0.1 wt% Au NPs on the surface of BiOBr nanosheets but almost kept unchanged when the amount of Au nanoparticles was further increased up to 0.5 wt%. This result validated the piezocatalytic effect of BiOBr nanosheets, and the decoration of Au NPs at an appropriate amount would largely enhance the piezocatalytic activity.

Photocatalytic CBZ degradation over all the as-synthesized catalysts was further conducted under visible light irradiation, as displayed in Fig. 5B. The photolysis of CBZ was also negligible. The pristine BiOBr could remove 6.6% of CBZ under visible light irradiation, and the efficiency of Au-BiOBr exhibited a slight improvement that up to 13.8% for 0.1 wt% Au-BiOBr. This result demonstrated the photocatalytic performance of BiOBr in response to visible light, and the existence of Au NPs was beneficial for photocatalytic CBZ degradation.

For piezo-photocatalysis, the performance of Au-BiOBr was significantly enhanced. Take 0.1 wt% Au-BiOBr as an example (Fig. 5C), it exhibited a limited photocatalytic activity (13.8%) and an unsatisfactory piezocatalytic (66.2%) activity on CBZ removal. With the coupling of ultrasonic vibration and visible light irradiation, 94.8% of CBZ was removed within 30 min, which was 81.0% higher than that of photocatalysis and 28.6% higher than that of piezocatalysis. Through the analysis of pseudo-first-order kinetics (Fig. 5D), the piezo-photocatalytic system achieved the highest reaction rate constant ($k_{(5)}$ = 0.0901 min^{-1}), which was about 1.73 times higher than the sum of
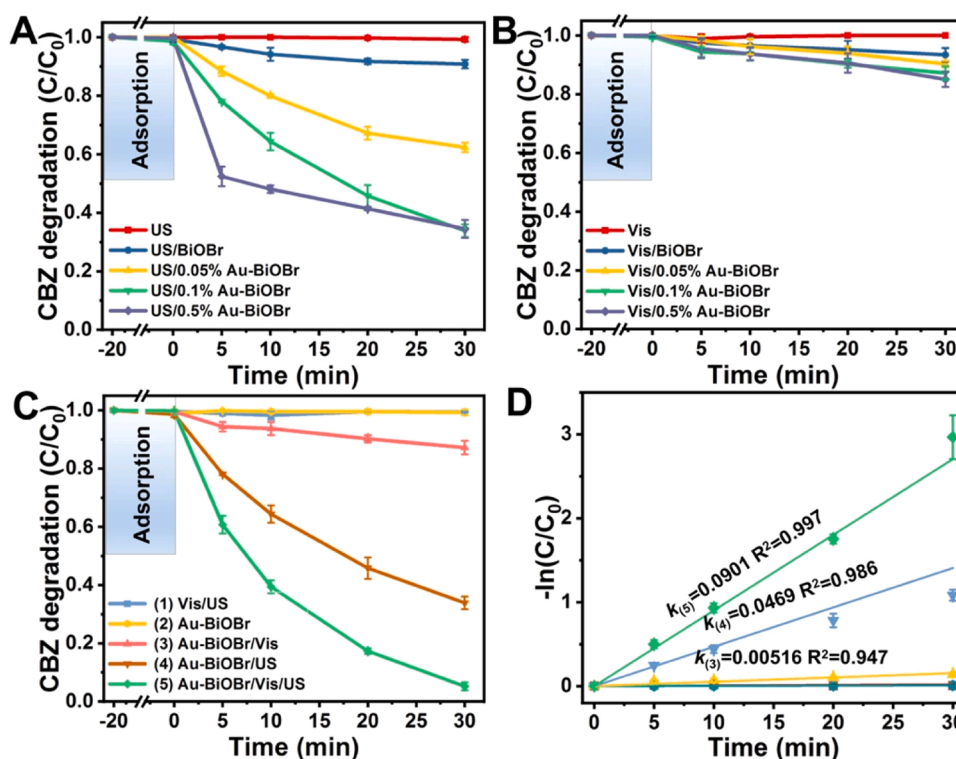

Fig. 5. (A) Piezocatalytic efficiency under ultrasonic vibration and (B) photocatalytic efficiency under visible light irradiation of CBZ degradation in the presence of x %—Au-BiOBr (x = 0, 0.05, 0.1, and 0.5); (C) CBZ degradation under different oxidation systems and (D) pseudo-first order kinetics of CBZ degradation (Experimental conditions: ultrasonic power = 100 W, light intensity = 100 mW cm^{-2}, Au-BiOBr dosage = 1 g L^{-1}, CBZ initial concentration = 5 mg L^{-1}).

piezocatalytic and photocatalytic systems. Additionally, the degradation efficiency of CBZ gradually increased with the increasing dosage of catalyst (Fig. S3). According to the findings, the piezo-potential played a vital part in the photocatalytic process, which might improve overall degrading performance greatly.

A series of experiments were then conducted to unveil the possible mechanisms. The reactive oxygen species (ROS) involved in piezo-, photo-, and piezo-photocatalysis were studied using electron paramagnetic resonance (EPR) techniques. DMPO or TEMP were respectively employed as the spin trapping agents. The obvious 1:1:1:1 quartet EPR signals were assigned as DMPO-$O_2^{\bullet-}$ adducts (Fig. 6A), the signals of the DMPO-$HO^{\bullet}$ adduct were the typical peaks with an intensity ratio of 1:2:2:1 (Fig. 6B), and the strong 1:1:1 triplet peak could be observed after adding TEMP was the TEMP-$^1O_2$ adduct signal (Fig. 6C) [36]. Under visible light, ultrasonic vibration, and simultaneous visible light/ultrasound irradiation, $O_2^{\bullet-}$, $HO^{\bullet}$, and $^1O_2$ may be generated over Au-BiOBr. Moreover, the EPR intensities of $O_2^{\bullet-}$, $HO^{\bullet}$, and $^1O_2$ from piezo-photocatalysis were the highest among all the systems. The degrading performances of piezocatalytic, photocatalytic, and piezo-photocatalytic systems were in line with these findings, suggesting that these ROS played a crucial role in piezo-photocatalytic CBZ degradation.

To get deeper insights into the degradation process and the predominant ROS for CBZ degradation over Au-BiOBr, quenching tests were carried out (Fig. 6D). EDTA-2Na, $K_2Cr_2O_7$, ascorbic acid (AA), tert-butyl alcohol (TBA), and L-histidine (L-His) were used to scavenge hole (h^+), electronic (e^-), superoxide anion radicals ($O_2^{\bullet-}$), hydroxyl radical ($HO^{\bullet}$), and singlet oxygen ($^1O_2$). The suppression of $K_2Cr_2O_7$ or EDTA-2Na was insignificant, meaning that e^- and h^+ played minor roles in CBZ elimination. With the addition of L-His and AA, the CBZ degradation efficiency decreased from 95.8% to 53.7% and 55.0%, suggesting that $^1O_2$ and $O_2^{\bullet-}$ participated in piezo-photocatalytic CBZ oxidation. When TBA

was introduced, the degradation efficiency declined markedly from 94.8% to 29.2%, indicating that $HO^{\bullet}$ was the primary ROS responsible for the CBZ degradation.

LC-TOF-MS was used to examine the intermediates of CBZ degradation, which contained P1~P19. Following that, possible CBZ degradation pathways were postulated, as shown in Fig. 7. The hydroxylation ring contraction (pathway I) and enhanced oxidation ring contraction (pathway II) were summarized and presented (pathway II) [37]. First, CBZ underwent hydroxylation and ring polycondensation to form P5, and then the oxidation and aldehyde loss of P5 formed intramolecular ring substances P9 and P6, respectively. Moreover, for pathway II, CBZ was easy to form P1 intermediate through oxidation and ring addition, and P1 intermediate could be oxidized through four reaction paths, namely: ring contraction to form P7, oxidation to form P10, and P11, and oxidation ring to contract to form P2. Then, P2, P7, P10, and P11 could be further oxidized to form smaller molecules. It was worth mentioning that P6 and P10 could also be attacked by ROS, causing C═C breakage and ring-opening, so that CBZ was oxidized into many small-molecule organics (P16–19) [38]. The LC-TOF-MS spectra of the products are shown in Fig. S4. In addition, the acute toxicity, developmental toxicity, bioaccumulation factor, and mutagenicity evaluation of CBZ and its degradation products were analyzed using Toxicity Estimation Software Tool with a Quantitative Structure Activity Relationship mathematical model (Fig. S5) [39,40].

The mechanism of piezo-photocatalytic CBZ degradation over Au-BiOBr was postulated in Scheme 2 based on the above analysis. Electron-hole pairs were generated over Au-BiOBr under visible light irradiation, meanwhile, the built-in electric field within the catalyst was enhanced by the ultrasonic vibration. In this process, the piezoelectric field could not only modulate the band structure alignment but also drive the separation and migration of photo-induced charges for surface reactions. Moreover, the decoration of Au NPs could enhance the
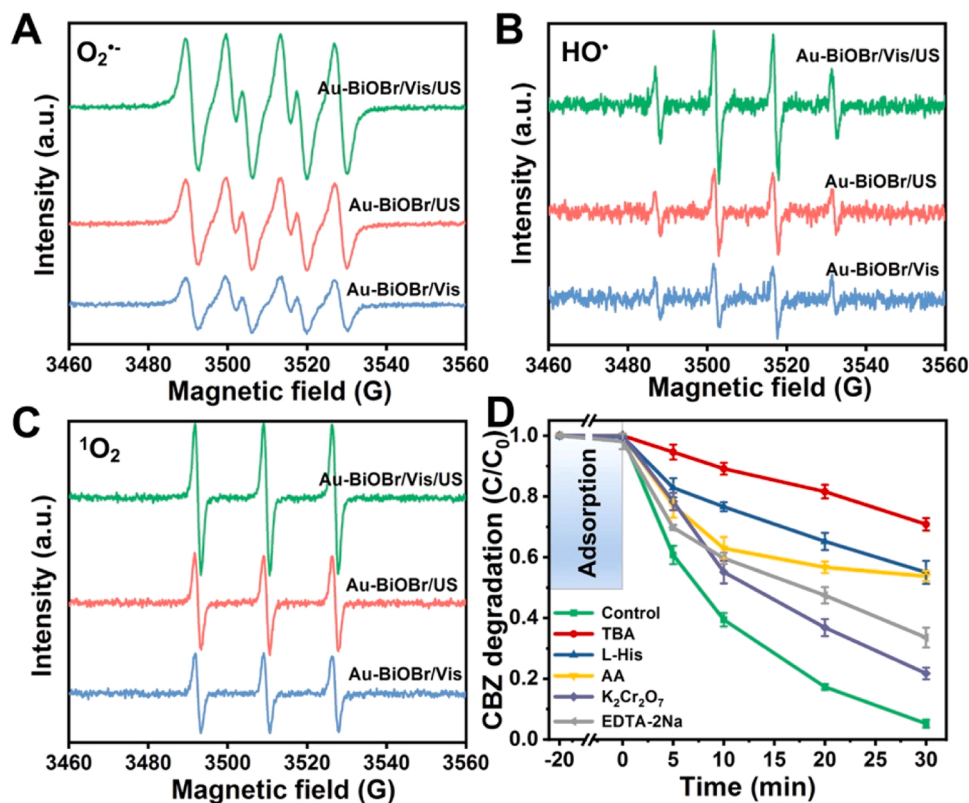

Fig. 6. EPR spectra of DMPO-$O_2^{\bullet-}$ (A), DMPO-$HO^{\bullet}$ (B) and TEMP-$^1O_2$ (C) in the Au-BiOBr/US/Vis, Au-BiOBr/US and Au-BiOBr/Vis system; (D) ROS scavenger experiments in the Au-BiOBr/US/Vis system for CBZ degradation (Experimental conditions: ultrasonic power = 100 W, light intensity = 100 mW cm^{-2}, Au-BiOBr dosage = 1 g L^{-1}, CBZ initial concentration = 5 mg L^{-1}, scavenger concentration = 5 mM).
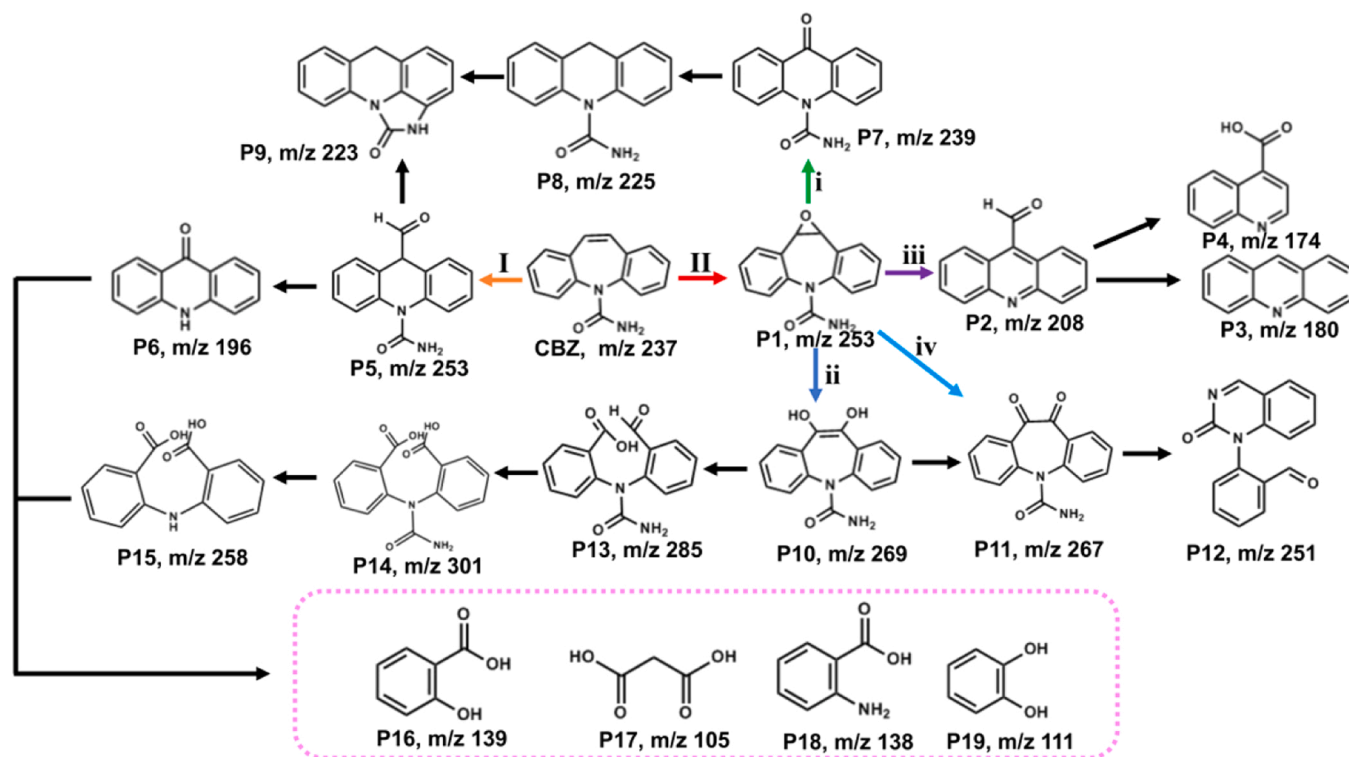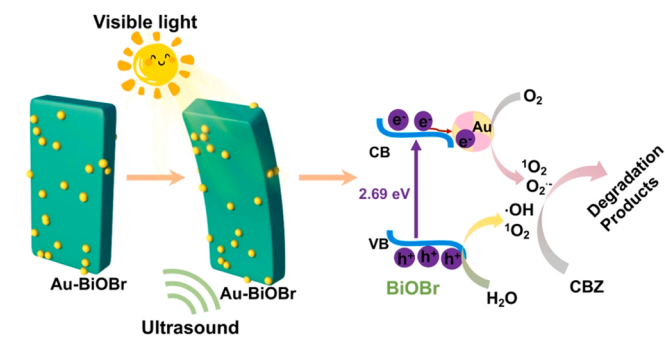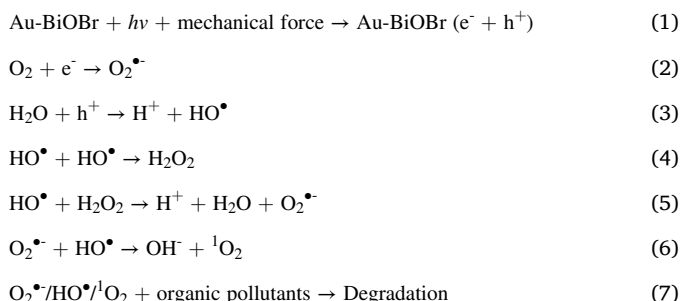
Fig. 7. Proposed pathways for CBZ degradation in the Au-BiOBr/US/Vis system.

Scheme 2. Piezo-enhanced photocatalytic mechanism of Au-BiOBr for CBZ degradation.

absorption of visible light via the SPR effect, as well as facilitate the interfacial charge transfer owing to the Schottky barriers. Therefore, sufficient charge carriers were generated and participated in CBZ degradation. The induced holes reacted with water molecules to produce $HO^\bullet$, while the electrons reacted with oxygen in the solution to produce $O_2^{\bullet-}$. The combination of $O_2^{\bullet-}$ and $HO^\bullet$ would further create $^1O_2$. These highly reactive ROS attacked the organic pollutants, leading to their removal (Eqs. (1–7)) [41–47].

$$Au\text{-}BiOBr + h\nu + \text{mechanical force} \rightarrow Au\text{-}BiOBr\ (e^- + h^+) \quad (1)$$

$$O_2 + e^- \rightarrow O_2^{\bullet-} \quad (2)$$

$$H_2O + h^+ \rightarrow H^+ + HO^\bullet \quad (3)$$

$$HO^\bullet + HO^\bullet \rightarrow H_2O_2 \quad (4)$$

$$HO^\bullet + H_2O_2 \rightarrow H^+ + H_2O + O_2^{\bullet-} \quad (5)$$

$$O_2^{\bullet-} + HO^\bullet \rightarrow OH^- + {}^1O_2 \quad (6)$$

$$O_2^{\bullet-}/HO^\bullet/{}^1O_2 + \text{organic pollutants} \rightarrow \text{Degradation} \quad (7)$$

3.4. Application of piezo-photocatalysis for CBZ degradation

With the mechanism in mind, the factors that could influence the piezo-photocatalytic system were explored. The role of the intensities of the applied stress was studied (Fig. S6). The removal efficiencies of CBZ within 30 min gradually increased from 79.1% (50 W) to 94.8% (100 W), which suggested that the higher applied stress originating from the more intense ultrasonic power would create stronger piezoelectric potential to facilitate ROS production. Moreover, the influence of the initial pH and different anions of the solution was investigated. As displayed in Fig. S7, CBZ degradation was promoted under acidic conditions, slightly inhibited under neutral conditions, and kept unchanged under alkaline conditions, probably because the moiety of -CONH₂ in the CBZ molecule was more susceptible to be decomposed in the acid solution [48]. Besides, in alkaline conditions, the CO_2 from the air and degradation process would be transformed into bicarbonate ions, which might compete with CBZ for reactive species, thus the photocatalytic degradation was restrained [49]. Fig. S8 showed that the existence of Cl^- or SO_4^{2-} did not affect the experiment, NO_3^- and HCO_3^- had a slight inhibitory effect. PO_4^{3-} could lead to obvious decay of the CBZ degradation efficiency probably because it might consume the oxidative radical species.

The potential of the catalyst in the practical application was evaluated in the cycling tests. The performance of recycled catalysts was comparable to that of new catalysts, as shown in Fig. 8A. The degrading efficiency of CBZ might still reach 89.2% after five cycles. This result demonstrated the high stability and good reproducibility of the Au-BiOBr piezo-photocatalysts. The XRD patterns of Au-BiOBr and Au-BiOBr-used did not change (Fig. S9), indicating that the crystal phase did not change during piezo-photocatalytic degradation of CBZ under Au-BiOBr/US/Vis system. It further proves that Au-BiOBr has excellent stability as a piezo-photocatalyst. The feasibility of the catalyst was further evaluated. The same experiments for CBZ removal were carried out in the rainwater and tap water spiked with CBZ. Fig. 8B showed that
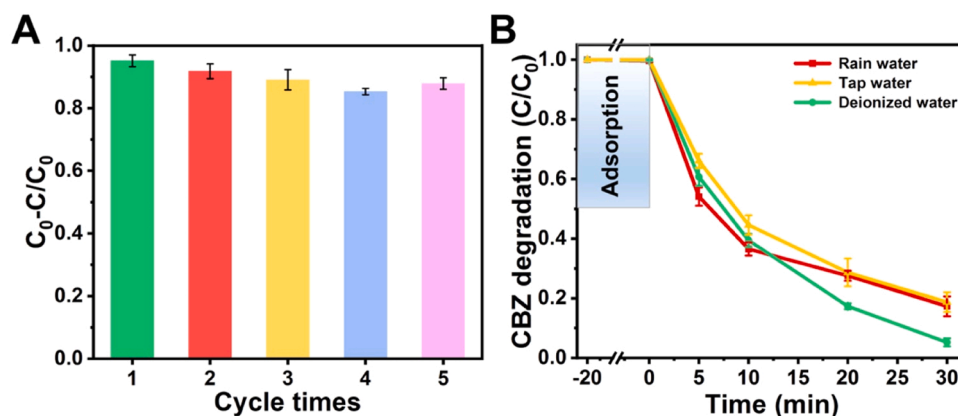
Fig. 8. (A) Recycling tests of CBZ degradation in Au-BiOBr piezo-photocatalytic process ; (B) Piezo-photocatalytic degradation of CBZ by Au-BiOBr in different water matrices (Experimental conditions: ultrasonic power = 100 W, light intensity = 100 mW cm^{-2}, Au-BiOBr dosage = 1 g L^{-1}, CBZ initial concentration = 5 mg L^{-1}).

about 82.8% and 81.3% of CBZ were removed within 30 min respectively via piezo-photocatalysis over Au-BiOBr. Although the performances were less efficient than that of deionized water, this result confirmed the great potential of the Au-BiOBr piezo-photocatalytic system for actual wastewater treatment.

4. Conclusion

In summary, efficient CBZ removal in wastewater was achieved over Au-BiOBr via piezo-photocatalysis. Compared with piezo- and photocatalysis, piezo-photocatalysis over Au-BiOBr exhibited significantly improved activity for CBZ degradation, in which 95.8% of CBZ was removed in the aqueous solution within 30 min. The application of mechanical stress amplified the built-in electric field for the separation of photo-induced charged carriers and moderated the band structure alignment for the surface reaction. Au modification improved visible light absorption through the SPR effect and accelerated charge transfer. Such a new piezo-photocatalytic process achieved the co-utilization of solar and mechanical energy in nature, providing an effective technology for environment purification.

CRediT authorship contribution statement

Jiayue Hu: Data curation, Investigation, Methodology, Writing – original draft. **Yanxi Chen**: Data curation, Methodology. **Yuanyi Zhou**: Data curation, Formal analysis. **Lixi Zeng**: Supervision, Writing – review & editing, Funding acquisition. **Yichao Huang**: Supervision, Writing – review & editing, Funding acquisition. **Shenyu Lan**: Formal analysis, Funding acquisition, Methodology. **Mingshan Zhu**: Conceptualization, Supervision, Writing – review & editing, Funding acquisition.

Declaration of Competing Interest

There are no conflicts to declare.

Acknowledgments

Appendix A. Supporting information

Supplementary data associated with this article can be found in the online version at doi:10.1016/j.apcatb.2022.121369.

References

[1] M.B. Starr, J. Shi, X. Wang, Piezopotential-driven redox reactions at the surface of piezoelectric materials, Angew. Chem. Int. Ed. 51 (2012) 5962–5966.

[2] H. Li, Y. Sang, S. Chang, X. Huang, Y. Zhang, R. Yang, H. Jiang, H. Liu, Z.L. Wang, Enhanced ferroelectric-nanocrystal-based hybrid photocatalysis by ultrasonic-wave-generated piezophototronic effect, Nano Lett. 15 (2015) 2372–2379.

[3] J.M. Wu, W.E. Chang, Y.T. Chang, C.K. Chang, Piezo-catalytic effect on the enhancement of the ultra-high degradation activity in the dark by single- and few-layers MoS$_2$ nanoflowers, Adv. Mater. 28 (2016) 3718–3725.

[4] J. Wu, N. Qin, D. Bao, Effective enhancement of piezocatalytic activity of BaTiO$_3$ nanowires under ultrasonic vibration, Nano Energy 45 (2018) 44–51.

[5] A. Biswas, S. Saha, N.R. Jana, ZnSnO$_3$ nanoparticle-based piezocatalysts for ultrasound-assisted degradation of organic pollutants, ACS Appl. Nano Mater. 2 (2019) 1120–1128.

[6] Y.-L. Liu, J.M. Wu, Synergistically catalytic activities of BiFeO$_3$/TiO$_2$ core-shell nanocomposites for degradation of organic dye molecule through piezophototronic effect, Nano Energy 56 (2019) 74–81.

[7] T.-M. Chou, S.-W. Chan, Y.-J. Lin, P.-K. Yang, C.-C. Liu, Y.-J. Lin, J.-M. Wu, J.-T. Lee, Z.-H. Lin, A highly efficient Au-MoS$_2$ nanocatalyst for tunable piezocatalytic and photocatalytic water disinfection, Nano Energy 57 (2019) 14–21.

[8] J. Yuan, X. Huang, L. Zhang, F. Gao, R. Lei, C. Jiang, W. Feng, P. Liu, Tuning piezoelectric field for optimizing the coupling effect of piezo-photocatalysis, Appl. Catal. B-Environ. 278 (2020), 119291.

[9] S. Tu, Y. Guo, Y. Zhang, C. Hu, T. Zhang, T. Ma, H. Huang, Piezocatalysis and piezo-photocatalysis: catalysts classification and modification strategy, reaction mechanism, and practical application, Adv. Funct. Mater. 30 (2020), 2005158.

[10] X. Huang, R. Lei, J. Yuan, F. Gao, C. Jiang, W. Feng, J. Zhuang, P. Liu, Insight into the piezo-photo coupling effect of PbTiO$_3$/CdS composites for piezo-photocatalytic hydrogen production, Appl. Catal. B-Environ. 282 (2021), 119586.

[11] M. Zhang, S. Nie, T. Cheng, Y. Feng, C. Zhang, L. Zheng, L. Wu, W. Hao, Y. Ding, Enhancing the macroscopic polarization of CdS for piezo-photocatalytic water splitting, Nano Energy 90 (2021), 106635.

[12] S. Lan, C. Yu, F. Sun, Y. Chen, D. Chen, W. Mai, M. Zhu, Tuning piezoelectric driven photocatalysis by La-doped magnetic BiFeO$_3$-based multiferroics for water purification, Nano Energy 93 (2021), 106792.

[13] J. Di, J. Xia, H. Li, S. Guo, S. Dai, Bismuth oxyhalide layered materials for energy and environmental applications, Nano Energy 41 (2017) 172–192.

[14] J. Li, Y. Yu, L. Zhang, Bismuth oxyhalide nanomaterials: layered structures meet photocatalysis, Nanoscale 6 (2014) 8473–8488.

[15] C. Liu, S. Mao, M. Shi, F. Wang, M. Xia, Q. Chen, X. Ju, Peroxymonosulfate activation through 2D/2D Z-scheme CoAl-LDH/BiOBr photocatalyst under visible light for ciprofloxacin degradation, J. Hazard. Mater. 420 (2021), 126613.

[16] X. Lv, D.Y.S. Yan, F.L.-Y. Lam, Y.H. Ng, S. Yin, A.K. An, Solvothermal synthesis of copper-doped BiOBr microflowers with enhanced adsorption and visible-light driven photocatalytic degradation of norfloxacin, Chem. Eng. J. 401 (2020), 126012.

[17] J. Jang, K. Kim, J. Yoon, C.B. Park, Piezoelectric materials for ultrasound-driven dissociation of Alzheimer's beta-amyloid aggregate structure, Biomaterials 255 (2020), 120165.

[18] R. Djellabi, M.F. Ordonez, F. Conte, E. Falletta, C.L. Bianchi, I. Rossetti, A review of advances in multifunctional XTiO$_3$ perovskite-type oxides as piezo-photocatalysts

for environmental remediation and energy production, J. Hazard. Mater. 421 (2022), 126792.

[19] X. Chen, X. Zhang, Y.-H. Li, M.-Y. Qi, J.-Y. Li, Z.-R. Tang, Z. Zhou, Y.-J. Xu, Transition metal doping BiOBr nanosheets with oxygen vacancy and exposed {102} facets for visible light nitrogen fixation, Appl. Catal. B-Environ. 281 (2021), 119516.

[20] H. Lei, H. Zhang, Y. Zou, X. Dong, Y. Jia, F. Wang, Synergetic photocatalysis/ piezocatalysis of bismuth oxybromide for degradation of organic pollutants, J. Alloy. Compd. 809 (2019) 151840.

[21] Y. Wei, Y. Zhang, W. Geng, H. Su, M. Long, Efficient bifunctional piezocatalysis of Au/BiVO₄ for simultaneous removal of 4-chlorophenol and Cr(VI) in water, Appl. Catal. B-Environ. 259 (2019), 118084.

[22] J. Dong, H. Li, P. Yan, L. Xu, J. Zhang, J. Qian, J. Chen, H. Li, A composite prepared from BiOBr and gold nanoparticles with electron sink and hot-electron donor properties for photoelectrochemical aptasensing of tetracycline, Mikrochim. Acta 186 (2019) 794.

[23] J. Wu, X. Li, W. Shi, P. Ling, Y. Sun, X. Jiao, S. Gao, L. Liang, J. Xu, W. Yan, C. Wang, Y. Xie, Efficient visible-light-driven CO₂ reduction mediated by defect-engineered BiOBr atomic layers, Angew. Chem. Int. Ed. 57 (2018) 8719–8723.

[24] H. Liu, X. Chang, X. Liu, G. Li, W. Zhang, T. An, Boosting the photocatalytic degradation of ethyl acetate by a Z-scheme Au–TiO₂@NH₂-UiO-66 heterojunction with ultrafine Au as an electron mediator, Environ. Sci. Nano 8 (2021) 2542–2553.

[25] D. Wu, S. Yue, W. Wang, T. An, G. Li, H.Y. Yip, H. Zhao, P.K. Wong, Boron doped BiOBr nanosheets with enhanced photocatalytic inactivation of Escherichia coli, Appl. Catal. B-Environ. 192 (2016) 35–45.

[26] D. Zhang, J. Li, Q. Wang, Q. Wu, High {001} facets dominated BiOBr lamellas: facile hydrolysis preparation and selective visible-light photocatalytic activity, J. Mater. Chem. A 1 (2013) 8622.

[27] Z. Wu, J. Shen, N. Ma, Z. Li, M. Wu, D. Xu, S. Zhang, W. Feng, Y. Zhu, Bi₄O₅Br₂ nanosheets with vertical aligned facets for efficient visible-light-driven photodegradation of BPA, Appl. Catal. B-Environ. 286 (2021), 119937.

[28] W. Zhang, G. Li, H. Liu, J. Chen, S. Ma, M. Wen, J. Kong, T. An, Photocatalytic degradation mechanism of gaseous styrene over Au/TiO₂@CNTs: Relevance of superficial state with deactivation mechanism, Appl. Catal. B-Environ. 272 (2020), 118969.

[29] X. Xiong, L. Ding, Q. Wang, Y. Li, Q. Jiang, J. Hu, Synthesis and photocatalytic activity of BiOBr nanosheets with tunable exposed {0 1 0} facets, Appl. Catal. B-Environ. 188 (2016) 283–291.

[30] J. Hu, C. Zhai, C. Yu, L. Zeng, Z.Q. Liu, M. Zhu, Visible light-enhanced electrocatalytic alcohol oxidation based on two dimensional Pt-BiOBr nanocomposite, J. Colloid Interface Sci. 524 (2018) 195–203.

[31] X.-Q. Deng, B. Zhu, X.-S. Li, J.-L. Liu, X. Zhu, A.-M. Zhu, Visible-light photocatalytic oxidation of CO over plasmonic Au/TiO₂: unusual features of oxygen plasma activation, Appl. Catal. B-Environ. 188 (2016) 48–55.

[32] H. Lei, Q. He, M. Wu, Y. Xu, P. Sun, X. Dong, Piezoelectric polarization promoted spatial separation of photoexcited electrons and holes in two-dimensional g-C₃N₄ nanosheets for efficient elimination of chlorophenols, J. Hazard. Mater. 421 (2022), 126696.

[33] X. Jia, J. Cao, H. Lin, M. Zhang, X. Guo, S. Chen, Transforming type-I to type-II heterostructure photocatalyst via energy band engineering: A case study of I-BiOCl/I-BiOBr, Appl. Catal. B-Environ. 204 (2017) 505–514.

[34] X. Li, J. Xiong, X. Gao, J. Huang, Z. Feng, Z. Chen, Y. Zhu, Recent advances in 3D g-C₃N₄ composite photocatalysts for photocatalytic water splitting, degradation of pollutants and CO₂ reduction, J. Alloy. Compd. 802 (2019) 196–209.

[35] H. Li, Y. Yu, M.B. Starr, Z. Li, X. Wang, Piezotronic-enhanced photoelectrochemical reactions in Ni(OH)₂-decorated ZnO photoanodes, J. Phys. Chem. Lett. 6 (2015) 3410–3416.

[36] W. Wang, H. Wang, G. Li, T. An, H. Zhao, P.K. Wong, Catalyst-free activation of persulfate by visible light for water disinfection: efficiency and mechanisms, Water Res. 157 (2019) 106–118.

[37] S. Franz, E. Falletta, H. Arab, S. Murgolo, M. Bestetti, G. Mascolo, Degradation of carbamazepine by photo(electro)catalysis on nanostructured TiO₂ meshes: transformation products and reaction pathways, Catalysts 10 (2020) 169.

[38] J. Cao, W. Nie, L. Huang, Y. Ding, K. Lv, H. Tang, Photocatalytic activation of sulfite by nitrogen vacancy modified graphitic carbon nitride for efficient degradation of carbamazepine, Appl. Catal. B-Environ. 241 (2019) 18–27.

[39] T. Puzyn, B. Rasulev, A. Gajewicz, X. Hu, T.P. Dasari, A. Michalkova, H.-M. Hwang, A. Toropov, D. Leszczynska, J. Leszczynski, Using nano-QSAR to predict the cytotoxicity of metal oxide nanoparticles, Nat. Nanotechnol. 6 (2011) 175–178.

[40] Y. Zhou, J. He, J. Lu, Y. Liu, Y. Zhou, Enhanced removal of bisphenol A by cyclodextrin in photocatalytic systems: degradation intermediates and toxicity evaluation, Chin. Chem. Lett. 31 (2020) 2623–2626.

[41] Q. Liu, D. Zhai, Z. Xiao, C. Tang, Q. Sun, C.R. Bowen, H. Luo, D. Zhang, Piezo-photoelectronic coupling effect of BaTiO₃@TiO₂ nanowires for highly concentrated dye degradation, Nano Energy 92 (2022), 106702.

[42] K. Fan, C. Yu, S. Cheng, S. Lan, M. Zhu, Metallic Bi self-deposited BiOCl promoted piezocatalytic removal of carbamazepine, Surf. Interfaces 26 (2021), 101335.

[43] S. Xu, L. Guo, Q. Sun, Z.L. Wang, Piezotronic effect enhanced plasmonic photocatalysis by AuNPs/BaTiO₃ heterostructures, Adv. Funct. Mater. 29 (2019), 1808737.

[44] D. Xiang, Z. Liu, M. Wu, H. Liu, X. Zhang, Z. Wang, Z.L. Wang, L. Li, Enhanced piezo-photoelectric catalysis with oriented carrier migration in asymmetric Au-ZnO nanorod array, Small 16 (2020), 1907603.

[45] S. Lan, X. Zeng, R.A. Rather, I.M.C. Lo, Enhanced trimethoxypyrimidine degradation by piezophotocatalysis of BaTiO₃/Ag₃PO₄ using mechanical vibration and visible light simultaneously, Environ. Sci. Nano 6 (2019) 554–564.

[46] H. Lei, M. Wu, Y. Liu, F. Mo, J. Chen, S. Ji, Y. Zou, X. Dong, Built-in piezoelectric field improved photocatalytic performance of nanoflower-like Bi₂WO₆ using low-power white LEDs, Chin. Chem. Lett. 32 (2021) 2317–2321.

[47] H. Lei, M. Wu, F. Mo, S. Ji, X. Dong, Y. Jia, F. Wang, Z. Wu, Efficiently harvesting the ultrasonic vibration energy of two-dimensional graphitic carbon nitride for piezocatalytic degradation of dichlorophenols, Environ. Sci. Nano 8 (2021) 1398–1407.

[48] X. Gao, X. Zhang, Y. Wang, S. Peng, B. Yue, C. Fan, Photocatalytic degradation of carbamazepine using hierarchical BiOCl microspheres: some key operating parameters, degradation intermediates and reaction pathway, Chem. Eng. J. 273 (2015) 156–165.

[49] H. Gong, W. Chu, M. Chen, Q. Wang, A systematic study on photocatalysis of antipyrine: catalyst characterization, parameter optimization, reaction mechanism and toxicity evolution to plankton, Water Res. 112 (2017) 167–175.